Helmholtz-Zentrum Dresden-Rossendorf (HZDR)

Clinical feasibility of single-source dual-spiral 4D dual-energy CT for proton treatment planning within the thoracic region

Wohlfahrt, P.; Troost, E. G. C.; Hofmann, C.; Richter, C.; Jakobi, A.;

Originally published:

July 2018

International Journal of Radiation Oncology Biology Physics 102(2018)4, 830-840

DOI: https://doi.org/10.1016/j.ijrobp.2018.06.044

Perma-Link to Publication Repository of HZDR:

https://www.hzdr.de/publications/Publ-26550

Release of the secondary publication
on the basis of the German Copyright Law § 38 Section 4.

CC BY-NC-ND

Title: Clinical feasibility of single-source dual-spiral 4D dual-energy CT for proton treatment planning within the thoracic region

Shortened Running Title: Dual-spiral 4D-DECT for thoracic region

ABSTRACT:

Purpose: Single-source dual-spiral dual-energy computed tomography (DECT) provides additional patient information but is prone to motion between both consecutively acquired CT scans. Here, the clinical applicability of dual-spiral time-resolved DECT (4D-DECT) for proton treatment planning within the thoracic region was evaluated.

Methods and Materials: Dual-spiral 4D-DECT scans of three lung-cancer patients were acquired. For temporally averaged datasets and 4 breathing phases, the geometrical conformity of 80/140kVp 4D-DECT scans before image post-processing was assessed by normalized cross correlation (NCC). Additionally, the conformity of the corresponding DECT-derived 58/79keV pseudo-monoenergetic CT datasets (MonoCTs) after image post-processing including deformable image registration (DIR) was determined. To analyze the reliability of proton dose calculation, clinical ($Plan_{Clin}$) and artificial worst-case ($Plan_{WorstCase}$, targeting diaphragm) treatment plans were calculated on 140kVp and 79keV datasets and compared with gamma analyses (0.1% dose-difference, 1mm distance-to-agreement criterion). The applicability of patient-specific DECT-based stopping-power-ratio (SPR) prediction was investigated and proton range shifts compared to the clinical heuristic CT-number-to-SPR conversion (HLUT) were assessed. Finally, the delineation variability of an experienced radiation oncologist was quantified on DECT-derived datasets.

Results: Dual-spiral 4D-DECT scans without DIR showed a high geometrical conformity with average NCC (±1SD) of 98.7(±1.0)% including all patient voxel or 88.2(±7.8)% considering only lung. DIR clearly improved the conformity leading to average NCC of 99.9(±0.1)% and 99.6(±0.5)%, respectively. $Plan_{Clin}$ dose distributions on 140kVp and 79keV datasets were similar with average gamma passing rate of 99.9% (99.2%-100%). The worst-case evaluation still revealed high passing rates (average: 99.3%, minimum: 92.4%). Clinically relevant mean range shifts of 2.2(±1.2)% were determined between patient-specific DECT-based SPR prediction and HLUT. The intra-observer delineation variability could be slightly reduced by additional DECT-derived datasets.

Conclusions: 79keV MonoCT datasets can be consistently obtained from dual-spiral 4D-DECT and are applicable for proton dose calculation. Patient-specific DECT-based SPR prediction performed appropriately and potentially reduces range uncertainty in proton therapy of lung-cancer patients.

MANUSCRIPT:

Introduction

Compared to single-energy computed tomography (SECT), the acquisition of two CT scans with different x-ray spectra (dual-energy CT, DECT) provides additional patient information and allows for the generation of a variety of image datasets useful for reducing metal artifacts, increasing image quality, improving tumor delineation and radiotherapy planning (1–3). As recently demonstrated in biological tissues and an anthropomorphic phantom, DECT enables a reliable prediction of stopping-power ratio (SPR) eventually leading to reduced uncertainty margins in proton therapy (4–7).

Several technical options of DECT are currently available. With a dedicated dual-source DECT scanner, both CT scans are recorded simultaneously, but the DECT information is only available in a field of view (FOV) of 30-35 cm (8). To gather DECT data in a FOV of 50 cm, typically required for radiotherapy planning in anatomical regions such as thorax, abdomen or pelvis, the different CT datasets can be obtained consecutively ("dual-spiral") by acquiring two separate CT scans one after the other, or almost simultaneously by continuous fast voltage switching, dual-layer detector or split-beam filter using a single-source CT scanner (2, 9–11). From the single-source techniques, the dual-spiral DECT approach allows for an independent tube current modulation, a larger energy separation and can be performed by standard CT scanners with appropriate software. However, dual-spiral DECT is prone to uncertainties due to patient motion during imaging (e.g., breathing, swallowing, heartbeat, gastro-intestinal peristalsis), which leads to different anatomies in the subsequent CT scans.

In this study, the clinical feasibility of dual-spiral time-resolved (4D) DECT for proton treatment planning within the thoracic region, i.e. in the presence of respiratory motion, was analyzed using a single-source CT scanner. For this purpose, the geometrical similarity of both individual 4D-DECT scans and the impact of DECT-derived datasets on dose calculation were determined. In addition, the applicability of patient-specific DECT-based stopping-power-ratio (SPR) prediction, aiming at more precise proton range estimation, and the intra-observer variability of tumor delineation on different DECT datasets were investigated.

Methods and Materials

Patient data

Three consecutive patients with advanced stage non-small-cell lung cancer (NSCLC, patient and tumor details in Table EAA, Supplement EA) participating in the phase II clinical trial XXX were selected in accordance with the approval of the local ethics committee XXX. Based on 4D-SECT scans, patient-specific internal gross tumor volumes (iGTVs) were defined by an experienced radiation oncologist. The clinical target volumes (CTVs) encompassed the iGTV and involved lymph nodes with 8 mm isotropic margin subsequently corrected for anatomical boundaries (Figure EAA(a), Supplement EA). Tumor motion was determined in cranio-caudal, left-right and anterior-posterior direction using the center-of-mass of the gross tumor volume (GTV) defined on each 4D-SECT respiratory phase (Table EAA, Supplement EA). Furthermore, the diaphragm motion was quantified based on the visible diaphragm line in exhalation and inhalation CT datasets.

CT acquisition

For treatment planning, 120 kVp 4D-SECT scans with 1×1×2 mm^3 voxel size were acquired at a single-source CT scanner SOMATOM Definition AS (Siemens Healthineers, Forchheim, Germany). An iterative reconstruction kernel with beam hardening correction concerning bone (Q34/5, SAFIRE) was applied to reduce image noise (adjusted by Siemens CARE Dose4D) and patient-size dependent CT number variations.

Respiratory motion during CT acquisition was recorded using a pressure belt system (ANZAI, Anzai Medical Co., Ltd, Tokyo, Japan) positioned onto the patient’s abdomen. Four CT datasets representing different breathing phases (maximum and slopes of inhalation and exhalation) were reconstructed using relative amplitude-based binning of CT projections according to the patient‘s breathing pattern. For a rotation time of 500 ms, this quick scan reconstruction results in a temporal resolution of approximately 250 ms for each respiratory phase per breathing period. Furthermore, a temporally averaged CT dataset was reconstructed using all CT projections.

To assess anatomical and motion changes during the course of treatment, these patients underwent weekly control 4D-SECT scans according to the clinical protocol. For the three selected patients, two dual-spiral 4D-DECT scans were acquired with similar total CT dose in between fractions 14-19 and 27-32, respectively. Each dual-spiral 4D-DECT scan comprises two 4D-SECT scans of 80 kVp and 140 kVp (Table EAB, Supplement EA), which were consecutively recorded within approximately 95 s each and a 10 s time delay for repositioning in between (Figure 1). Image reconstruction was performed as described previously using the same nominal relative amplitude-based binning.

4D-DECT image post processing

The application syngo.CT DE Monoenergetic Plus of the Siemens image post-processing software syngo.via was applied on dual-spiral 4D-DECT scans to create pseudo-monoenergetic CT datasets (MonoCTs) of 58 keV, 79 keV and 170 keV. The 58/79 keV datasets comprised similar attenuation information as the initial 80/140 kVp CT scans, but were aligned by deformable image registration (DIR) and contained less image noise (2). Material parameters, such as relative electron density (RED), obtained from 170 keV MonoCT, and relative photon cross section (RCS), derived by dividing 79 keV MonoCT by RED, were determined and used to calculate SPR datasets (12). This patient-specific SPR prediction approach, referred to as RhoSigma, was implemented as described in XXX.

Treatment planning

Passively scattered proton treatment plans with three fields were generated in XiO (Elekta AB, Stockholm, Sweden) using the average planning SECT scan and the clinical heuristic CT-number-to-SPR conversion (HLUT) of our institution (XXX). Average dose to the CTV was aimed at 66 Gy(RBE) using a relative biological effectiveness (RBE) of 1.1. For hardware preparation and range/modulation determination, the iGTV was assigned to a mean density derived from the GTV of each 4D-SECT breathing phase. Treatment uncertainty was included in aperture margins and compensator smearing of 10 mm as well as range uncertainty of (3.5% + 2 mm). Dose calculations were performed without density assignment to the iGTV using a 1×1×1 mm^3 dose grid and a pencil-beam algorithm.

Additionally, worst-case-scenario plans were generated using a single lateral proton beam covering an artificial target volume that encompassed the diaphragm, the anatomical region where the highest motion occurred (Figure EAA(b), Supplement EA).

4D-DECT scan similarity

The geometrical similarity of dual-spiral DECT datasets was assessed visually and by normalized cross correlation (NCC)

$$\mathrm{NCC} = \frac{\sum_{\mathrm{ROI}} H_i \, H_j}{\sqrt{\sum_{\mathrm{ROI}} {H_i}^2 \sum_{ROI} {H_j}^2}} \cdot 100\% \qquad (1)$$

including CT numbers of both datasets, H_i and H_j, within region of interests (ROIs), *e.g.*, patient body, CTV, heart and total lung. NCC of 100% declares perfect agreement and 0% no conformity.

To analyze patient datasets of different x-ray attenuation, CT numbers of 80 kVp/58 keV were transferred to 140 kVp/79 keV using a linear conversion table established on a DECT scan of a rigid thorax phantom (Figure EBA, Supplement EB). Subsequently, NCC values were determined for 4D-DECT datasets before (80/140 kVp) and after (58/79 keV) DIR. The sensitivity of NCC was estimated by comparing a patient dataset shifted by 1, 2, 3, 5, 7, 10 mm in cranio-caudal direction with the non-shifted dataset to correlate geometrical deviation with NCC (Table EBA, Figure EBB Supplement EB). Furthermore, breathing patterns during dual-spiral 4D-DECT were compared with regard to their variability and the feasibility to identify differences in DECT scans.

Reliability of 79 keV MonoCT

To assess the influence of anatomical changes in between both 4D-DECT scans on dose calculation, the clinical and worst-case-scenario plans were recalculated on DECT-derived 79 keV MonoCT datasets and their associated 140 kVp SECT scans as reference in RayStation 6.0 (RaySearch Laboratories, Stockholm, Sweden) using the clinical HLUT (XXX). For average CT datasets and four breathing phases, differences in dose distributions were quantified by voxelwise dose deviations and two-dimensional gamma analysis with 1 mm distance-to-agreement and 0.1% dose-difference, $\gamma(1\text{mm},0.1\%)$, or 1% dose-difference criterion, $\gamma(1\text{mm},1\%)$, respectively (13). Furthermore, deviations in dose-volume histograms (DVHs) were evaluated for CTV and the organs at risk (OARs) heart, esophagus and total lung.

Application of patient-specific DECT-based SPR prediction

Since a direct import of SPR datasets for dose calculation in RayStation 6.0 is not possible, XiO was used to recalculate clinical treatment plans on (a) 79 keV MonoCT datasets applying the clinical HLUT and (b) SPR datasets derived by RhoSigma. Deviations in dose distribution were evaluated as described above for average CT datasets and breathing phases. To assess water-equivalent range shifts (ΔR_{WET}) between the RhoSigma and HLUT approach, depth-dose curves in beam direction traversing the CTV with 1 mm spacing were analyzed for each treatment field using an in-house implemented ray-tracing algorithm (XXX). For this purpose, the distal range at 80% of the reference dose was used as proton range.

For average CT datasets, the correlation of CT number and SPR obtained from RhoSigma were determined within the irradiated volume (20% isodose) and illustrated as frequency distribution (Figure 4b).

Tumor delineation using DECT

To analyze the impact of image contrast on tumor detection, an experienced radiation oncologist delineated the GTV of each patient on several average CT datasets. First, only the 79 keV MonoCT dataset was used, which represents the clinical standard procedure. In a second step, the RED and RCS datasets were jointly provided. To quantify the intra-observer variability, the delineations were repeated once after a week. The conformity of GTV contours was assessed by Jaccard index and Hausdorff distance defined as 95th quantile of distances for each patient (14, 15).

Results

Similarity of dual-spiral 4D-DECT

Only small differences were found between the dual-spiral 80/140 kVp 4D-DECT scans, which are mainly visible on the upper anterior thorax wall and are in accordance with the assessed variability of the breathing amplitudes (Figure ECA, Supplement EC). Changes in respiratory frequency were rather minor and virtually adjusted in image reconstruction. For average CT datasets, the patient body, CTV and heart revealed a $\mathrm{NCC} > 99.5\%$ and both lungs a $\mathrm{NCC} > 95\%$ (Table 1), indicating mean shifts between each scan equivalent to global shifts of less than 0.5 mm (Table EBA, Supplement EB). CT datasets of individual breathing phases showed slightly less similarity and the respective NCC corresponded to shifts of approximately 1 mm. This confirms the general high resemblance of dual-spiral 4D-DECT scans. NCC values for all patients and ROIs are given in Tables EBB-EBE, Supplement EB.

Patient movement had a larger impact than breathing: In one case, the patient had to cough considerably at the end of the first 4D-DECT scan, which changed his overall body position especially visible by an altered position of the vertebrae. The NCC dropped markedly to 98.7% for body and 88.4% for total lung, similar to a global shift of approximately 1.3 mm between the average 80/140 kVp datasets.

The differences caused by respiratory motion could almost be completely resolved by DIR, which was applied between 80/140 kVp datasets prior to further image post-processing. This resulted in increased NCC values between 58/79keV datasets, indicating shifts less than 0.1 mm, also for the coughing patient (Table 1, Figure 2).

In contrast, movement of other organs or structures, *e.g.* the esophagus or gas in the stomach, and irregularities in respiratory motion visible at the diaphragm could not be sufficiently corrected by DIR and led to remaining uncertainties in DECT-derived datasets. Since these volumes were quite small, they did not influence the NCC, but were well visible as bright artifacts in DECT-derived datasets, such as RED and SPR (Figure EDA, Supplement ED).

Feasibility of dose calculation on 79 keV MonoCT datasets

Dose distributions calculated on 140 kVp and DECT-derived 79 keV MonoCT datasets were highly similar leading to no differences in DVH parameters of OARs and CTV. For clinical treatment plans, maximum dose differences ranged between 0.2-0.6 Gy(RBE) resulting in $\gamma(1\text{mm},1\%) = 100\%$ for all average CT datasets and breathing phases. Even the tighter gamma criterion revealed average and minimum gamma passing rates of $\gamma_{\text{avg}}(1\text{mm},0.1\%) = 99.9\%$ and $\gamma_{\text{min}}(1\text{mm},0.1\%) = 99.2\%$.

Dose differences of up to 2.2 Gy(RBE) were obtained for worst-case scenarios, which led to remainingly high gamma passing rates of $\gamma_{\text{avg}}(1\text{mm},0.1\%) = 99.3\%$, $\gamma_{\text{min}}(1\text{mm},0.1\%) = 92.4\%$ and $\gamma_{\text{min}}(1\text{mm},1\%) = 98.0\%$. DVH parameters of OARs and CTV did not change.

Application of patient-specific DECT-based SPR prediction

Dose distributions calculated on 79 keV MonoCT and SPR datasets derived by RhoSigma revealed dose differences of up to 21.2 Gy(RBE) and an average gamma passing rate of $\gamma_{\text{avg}}(1\text{mm},1\%) = 82.8\%$. Overall and field-specific dose differences and their associated water-equivalent range shifts are illustrated in Figure 3. The impact on DVH parameters depended on patient anatomy and beam direction. The volume of the contralateral lung receiving 5 Gy(RBE) increased by 4% for one patient with one beam exiting into this region (Figure 3b), while the other two patients showed smaller changes of 1.5% and 0%, respectively. Target coverage, defined by the dose applied to 98% of the CTV, remained stable for all patients with reductions of only 0.1%, which demonstrates the robustness of the treatment planning approach against CT calibration uncertainty.

Considering all investigated depth-dose profiles obtained for all 4D-DECT datasets of each patient, a mean relative water-equivalent range shift (± standard deviation) of 2.2% ($\pm 1.2\%$) between the RhoSigma and HLUT approach was determined (Figure 4c). This corresponds to a mean absolute water-equivalent range shift of 2.9 mm (± 1.4 mm). These deviations were mainly caused by the HLUT which predicts larger SPR for muscles ($H \approx 40$ HU), trabecular bone ($100\text{ HU} \leq H \leq 300\text{ HU}$) and tissue mixtures with CT numbers ranging from -400 HU to 100 HU (Figure 4b). Accordingly, range shifts within a treatment field depend on the distribution of tissues traversed in beam direction and result in an intra-patient variability of 1.1%, which is clearly larger than the inter-patient variation of 0.1% (Figure 4a). Furthermore, range shifts were similar using the average CT dataset (2.3%) or a breathing phase (2.2%) for dose calculation.

GTV delineation

The intra-observer variability of GTV delineation could be slightly reduced by jointly using DECT-derived RED and RCS datasets rather than only the 79 keV MonoCT dataset (Figure

5). This was indicated by an increased mean Jaccard index (± standard deviation) of $82.6\%\ (\pm 2.1\%)$ compared to $80.3\%\ (\pm 4.9\%)$ and reduced mean Hausdorff distance of $3.8\ \text{mm}\ (\pm 1.1\ \text{mm})$ compared to $4.5\ \text{mm}\ (\pm 0.8\ \text{mm})$.

The GTV contours (fusion of repeated delineations) obtained on 79 keV MonoCT or RED/RCS datasets revealed a mean Jaccard index of $82.8\%\ (\pm 4.2\%)$ and Hausdorff distance of $3.9\ \text{mm}\ (\pm 0.5\ \text{mm})$.

Discussion

The presented study demonstrated the feasibility of dual-spiral 4D-DECT for radiotherapy planning in the thoracic region in terms of anatomical and dosimetrical consistency and outlined the large variety of possibilities for potentially improving tumor delineation and CT-based SPR prediction in proton therapy. This approach assumes a high similarity in motion and anatomy between both consecutive 4D-DECT scans. Guckenberger *et al*. (16) demonstrated that multiple 4D-SECT scans acquired within a 30 minute timeframe are equally representative for treatment planning for the majority of patients. Malinowski *et al*. (17) and Shah *et al*. (18) showed that relevant changes in respiratory motion usually occur after a longer time period as opposed to that required for dual-spiral 4D-DECT. For the patients investigated in the presented study, the differences between both 4D-DECT scans were found to be small. This allows for reliable image post-processing and eventually clinical application of dual-spiral 4D-DECT. Thus, as recently shown for brain-tumor and prostate-cancer patients (3), patient-specific DECT-based SPR prediction is also clinically feasible within the thoracic region.

4D-DECT provides more detailed patient information of crucial importance for three aspects of proton therapy. First, patient-specific SPR predictions consider tissue heterogeneity and patient variability, which cannot be adequately incorporated using the clinical state-of-the-art HLUT approach, and thus can lead to more reliable dose calculation in proton treatment planning (19, 20). The impact of using a pencil-beam dose algorithm instead of a more sophisticated Monte Carlo approach, which limits the precision of the presented dose calculations in heterogeneous anatomical regions as thorax (21), remains small in relative dose comparisons and would not change the conclusions we draw here.

Second, multiple datasets of different image contrast can be derived from DECT, which might support a more reliable target delineation. For the evaluated NSCLC patient cohort, the intra-observer variability of GTV delineation was slightly influenced by different DECT datasets. To finally judge the effect on delineation precision, a further comprehensive evaluation should include more patients, more physicians to assess the inter-observer variability and additional DECT-derived datasets to obtain optimal settings. As delineation of lung tumors is supposed to be rather robust owing to the large CT image contrast to surrounding tissues, such a study should also be extended to other tumor entities to analyze site-specific advantages.

Third, information about motion variability can be gained. Differences in breathing pattern over time are a general challenge in radiotherapy, where a 4D-SECT scan acquired days to weeks before treatment is used as single baseline for therapy. The comparison of the two CT datasets of a dual-spiral 4D-DECT scan can contribute to identify patients with irregular and non-representative breathing patterns or to illustrate esophageal motion and regions of severe gastro-intestinal peristalsis during CT acquisition. These patients might currently not be eligible for accurate DECT-based SPR prediction. However, since SPR datasets visualize regions of severe motion, an additional image-based algorithm can be developed in future to detect such motion-induced changes and consider them in SPR prediction. Even if too large differences occur during dual-spiral 4D-DECT acquisition, hampering the calculation of reliable DECT-based datasets, still important information about motion variability and reliability regarding iGTV delineation for treatment planning can be gathered. Both consecutive 4D-DECT scans could also be included in robust optimization techniques including breathing variability in treatment planning (22–24). Furthermore, this could also highlight patients, who may require the application of a breathing suppression technique, a close intra-therapeutic monitoring to ensure short-term plan adaptations or even real-time imaging during treatment (25). Standard SECT-based dose calculation can always be performed without limitations using only the 140 kVp dataset. Thus, DECT scans of patients will always provide additional information without being disadvantageous for the individual patient.

In this proof-of-principle study, only six 4D-DECT scans of three advanced stage NSCLC patients with small tumor motion were investigated. As most advanced stage NSCLC tumors do not move significantly (26), the presented results will be valid for the majority of these patients. A comprehensive analysis of 4D-DECT is currently planned including more patients with larger tumor motion, which may have a larger impact on dose calculation as shown for the diaphragm region.

Conclusions

Single-source dual-spiral DECT can be reliably combined with time-resolved image acquisition, which results in 4D-DECT applicable for proton treatment planning within the thoracic region. Motion-induced changes in patient anatomy between the acquisition of both 4D-DECT scans are effectively minimized by deformable image registration allowing for a consistent DECT-based SPR prediction. Remaining motion artifacts in SPR datasets due to unstable breathing patterns indicate potential uncertainties during treatment, which can be considered in treatment planning using both 4D-DECT datasets individually.

REFERENCES

1. van Elmpt W, Landry G, Das M, *et al.* Dual energy CT in radiotherapy: Current applications and future outlook. *Radiother. Oncol.* 2016;119:137–144.

2. Wohlfahrt P, Möhler C, Hietschold V, *et al.* Clinical implementation of dual-energy CT for proton treatment planning on pseudo-monoenergetic CT scans. *Int. J. Radiat. Oncol. Biol. Phys.* 2017;97:427–434.

3. Wohlfahrt P, Möhler C, Stützer K, *et al.* Dual-energy CT based proton range prediction in head and pelvic tumor patients. *Radiother. Oncol.* 2017;125:526–533.

4. Taasti VT, Michalak GJ, Hansen DC, *et al.* Validation of proton stopping power ratio estimation based on dual energy CT using fresh tissue samples. *Phys. Med. Biol.* 2017.

5. Bär E, Lalonde A, Zhang R, *et al.* Experimental validation of two dual-energy CT methods for proton therapy using heterogeneous tissue samples. *Med. Phys.* 2017.

6. Möhler C, Russ T, Wohlfahrt P, *et al.* Experimental verification of stopping-power prediction from single- and dual-energy computed tomography in biological tissues. *Phys. Med. Biol.* 2018.

7. Wohlfahrt P, Möhler C, Richter C, *et al.* Evaluation of Stopping-Power Prediction by Dual- and Single-Energy Computed Tomography in an Anthropomorphic Ground-Truth Phantom. *Int. J. Radiat. Oncol.* 2018;100:244–253.

8. Flohr TG, McCollough CH, Bruder H, *et al.* First performance evaluation of a dual-source CT (DSCT) system. *Eur. Radiol.* 2006;16:256–268.

9. Kalender WA, Perman WH, Vetter JR, *et al.* Evaluation of a prototype dual-energy computed tomographic apparatus. I. Phantom studies. *Med. Phys.* 1986;13:334–339.

10. Heismann BJ, Wirth S, Janssen S, *et al.* Technology and image results of a spectral CT system. *Med. Imaging 2004 Phys. Med. Imaging, Pts 1 2*. 2004;5368:52–59.

11. Almeida IP, Schyns LEJR, Öllers MC, *et al.* Dual-energy CT quantitative imaging: a comparison study between twin-beam and dual-source CT scanners. *Med. Phys.* 2017;44:171–

179.

12. Möhler C, Wohlfahrt P, Richter C, *et al.* Range prediction for tissue mixtures based on dual-energy CT. *Phys. Med. Biol.* 2016;61:N268–N275.

13. Low DA, Harms WB, Mutic S, *et al.* A technique for the quantitative evaluation of dose distributions. *Med. Phys.* 1998;25:656–61.

14. Jaccard P. The distribution of the flora in the alphine zone. *New Phytol.* 1912;XI:37–50.

15. Taha AA, Hanbury A. Metrics for evaluating 3D medical image segmentation: analysis, selection, and tool. *BMC Med. Imaging*. 2015;15:29.

16. Guckenberger M, Wilbert J, Meyer J, *et al.* Is a Single Respiratory Correlated 4D-CT Study Sufficient for Evaluation of Breathing Motion? *Int. J. Radiat. Oncol. Biol. Phys.* 2007;67:1352–1359.

17. Malinowski K, McAvoy TJ, George R, *et al.* Incidence of changes in respiration-induced tumor motion and its relationship with respiratory surrogates during individual treatment fractions. *Int. J. Radiat. Oncol. Biol. Phys.* 2012;82:1665–1673.

18. Shah C, Grills IS, Kestin LL, *et al.* Intrafraction variation of mean tumor position during image-guided hypofractionated stereotactic body radiotherapy for lung cancer. *Int. J. Radiat. Oncol. Biol. Phys.* 2012;82:1636–1641.

19. Yang M, Virshup G, Clayton J, *et al.* Theoretical variance analysis of single- and dual-energy computed tomography methods for calculating proton stopping power ratios of biological tissues. *Phys. Med. Biol.* 2010;55:1343–1362.

20. Wohlfahrt P, Möhler C, Greilich S, *et al.* Comment on: Dosimetric comparison of stopping-power calibration with dual-energy CT and single-energy CT in proton therapy treatment planning [Med. Phys. 43(6), 2845-2854 (2016)]. *Med. Phys.* 2017;44:5533–5536.

21. Grassberger C, Daartz J, Dowdell S, *et al.* Quantification of proton dose calculation accuracy in the lung. *Int. J. Radiat. Oncol. Biol. Phys.* 2014;89:424–430.

22. Li H, Zhang X, Park P, *et al.* Robust optimization in intensity-modulated proton therapy

to account for anatomy changes in lung cancer patients. *Radiother. Oncol.* 2015;114:367–372.

23. Van Der Voort S, Van De Water S, Perkó Z, *et al.* Robustness Recipes for Minimax Robust Optimization in Intensity Modulated Proton Therapy for Oropharyngeal Cancer Patients. *Int. J. Radiat. Oncol. Biol. Phys.* 2016;95:163–170.

24. Stützer K, Lin A, Kirk M, *et al.* Superiority in Robustness of Multifield Optimization Over Single-Field Optimization for Pencil-Beam Proton Therapy for Oropharynx Carcinoma: An Enhanced Robustness Analysis. *Int. J. Radiat. Oncol.* 2017;99:738–749.

25. Péguret N, Ozsahin M, Zeverino M, *et al.* Apnea-like suppression of respiratory motion: First evaluation in radiotherapy. *Radiother. Oncol.* 2016;118:220–226.

26. Li Y, Kardar L, Li X, *et al.* On the interplay effects with proton scanning beams in stage III lung cancer. *Med. Phys.* 2014;41:21721.

TABLES

Table 1: NCC values for the investigated lung-cancer patient cohort.

Mean normalized correlation coefficient (NCC) ± 1 standard deviation[*] / %				
	80 kVp vs 140 kVp			
	Average CT		CT Phases	
	Body	Lungs	Body	Lungs
Patient cohort[#]	99.64 ± 0.09	97.36 ± 0.57	98.90 ± 0.15	89.09 ± 3.05
Coughing patient	97.26	88.35	96.42 ± 0.08	72.47 ± 6.37
	58 keV vs 79 keV			
	Average CT		CT Phases	
	Body	Lungs	Body	Lungs
Patient cohort[#]	99.90 ± 0.02	99.84 ± 0.03	99.85 ± 0.04	99.61 ± 0.15
Coughing patient	99.80	99.80	99.59 ± 0.15	98.97 ± 0.70

[*] determined independent from the individual patient

[#] except for the dual-energy CT dataset of the coughing patient

FIGURES

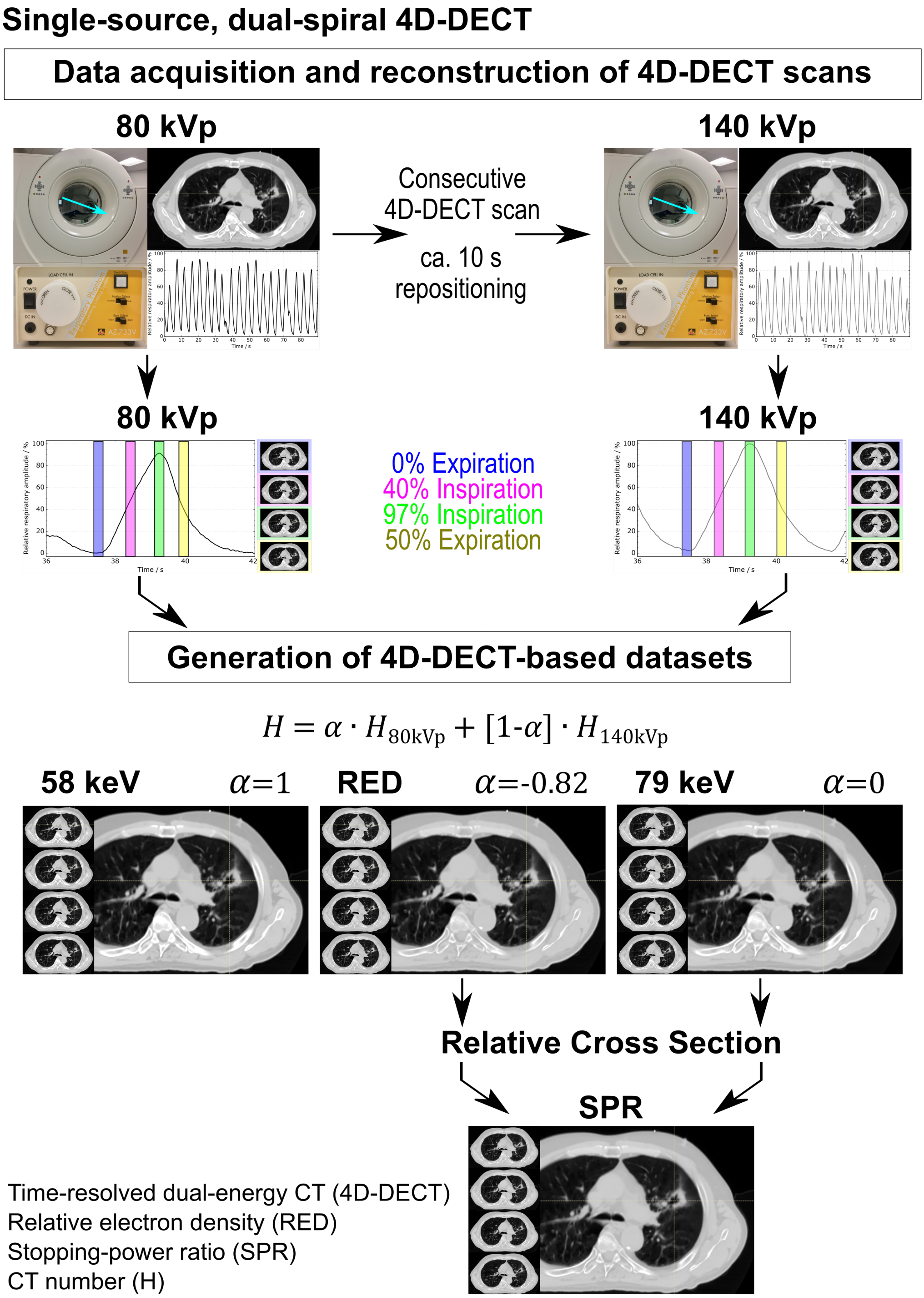

Figure 1: Methodology of dual-spiral 4D-DECT and image reconstruction.

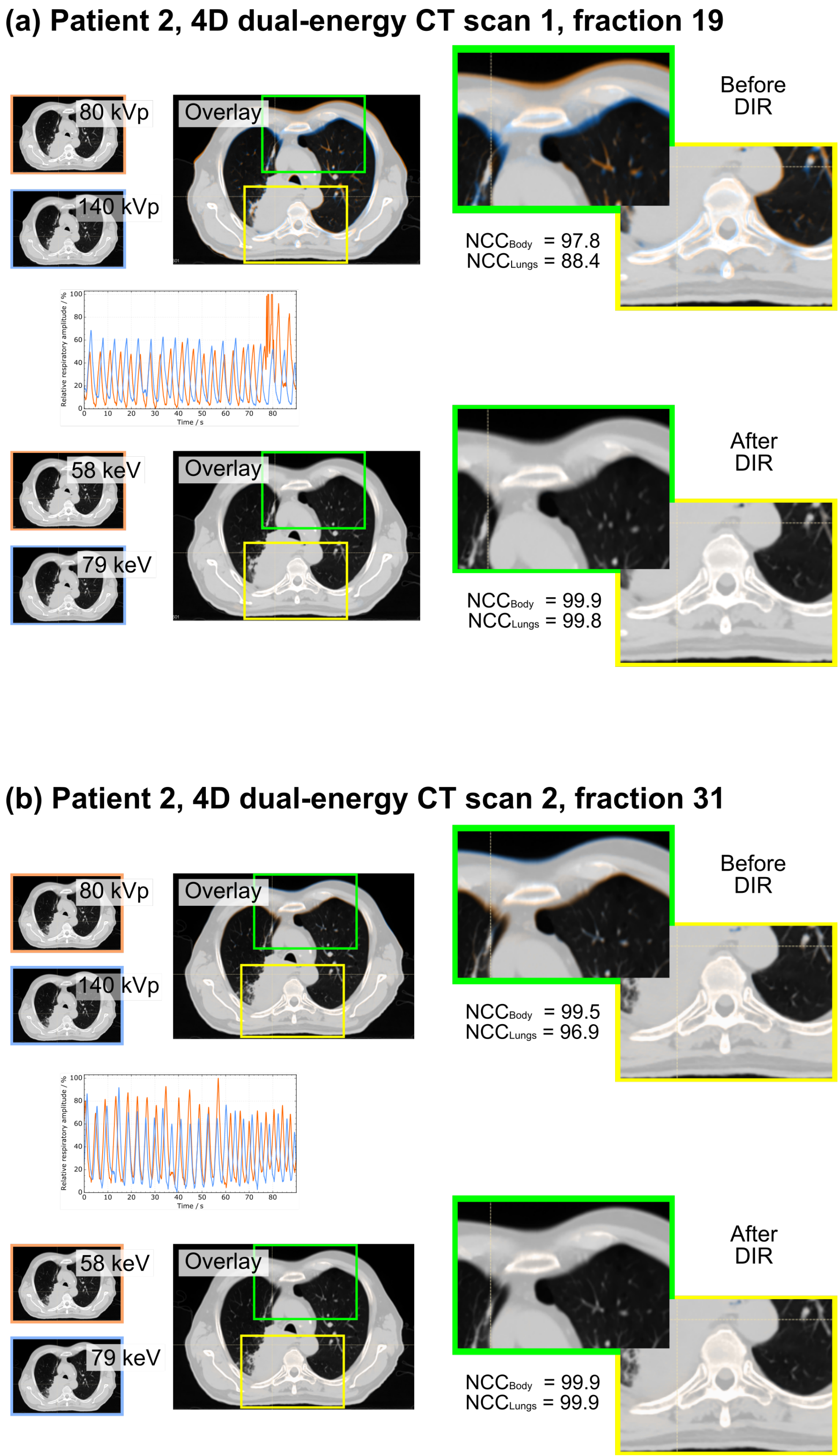

Figure 2: Dual-spiral 4D-DECT datasets of patient 2 before and after deformable image registration (DIR).

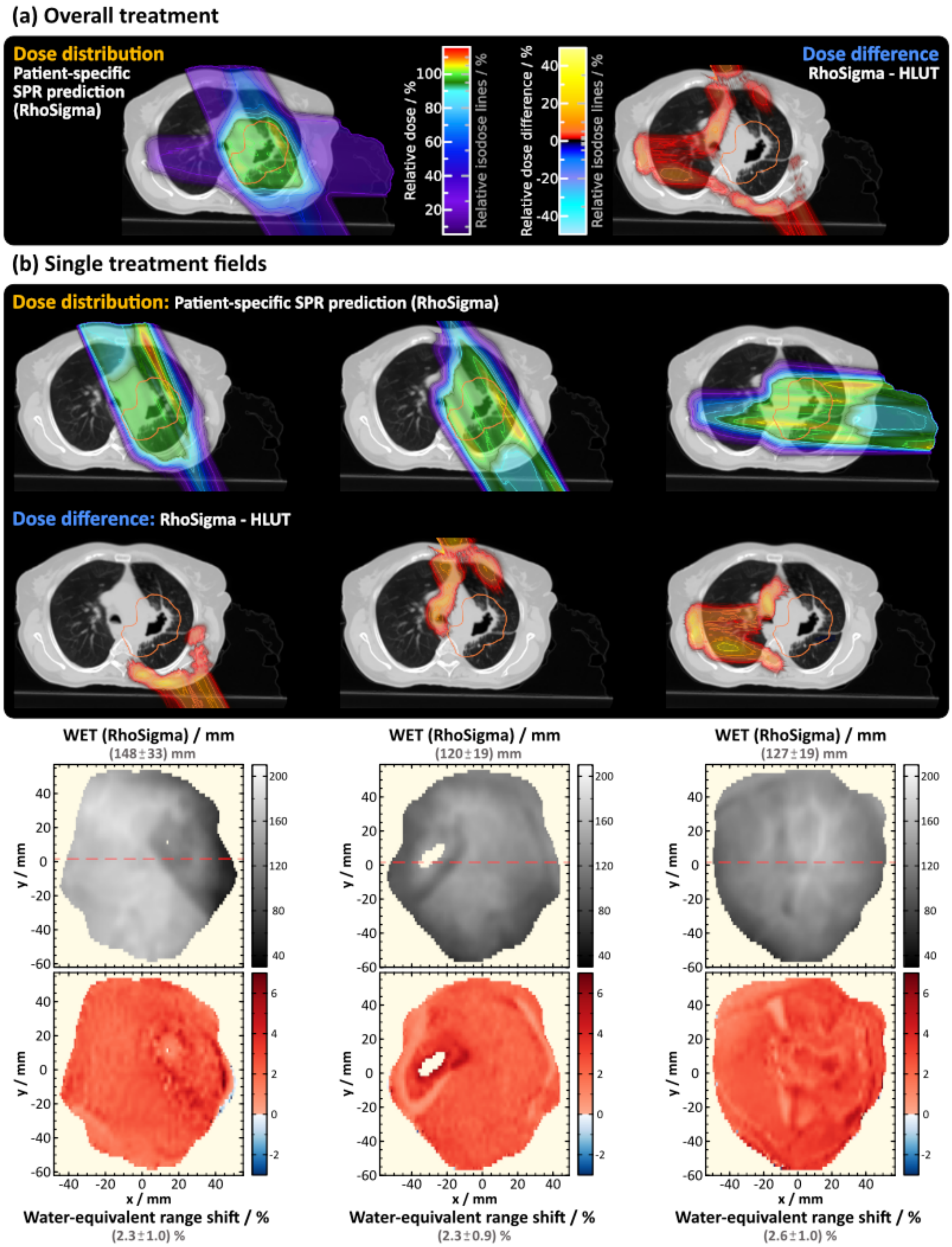

Figure 3: Dose distribution and difference between patient-specific prediction of stopping-power ratio (SPR) and Hounsfield look-up table (HLUT) for (a) the overall treatment and (b) single treatment fields of patient 1. Assessment of water-equivalent thickness and relative range shifts in beam direction for each treatment field. (Mean ± standard deviation) is stated for each beam's eye view (BEV). The red dashed line indicates the axial CT slice in BEV.

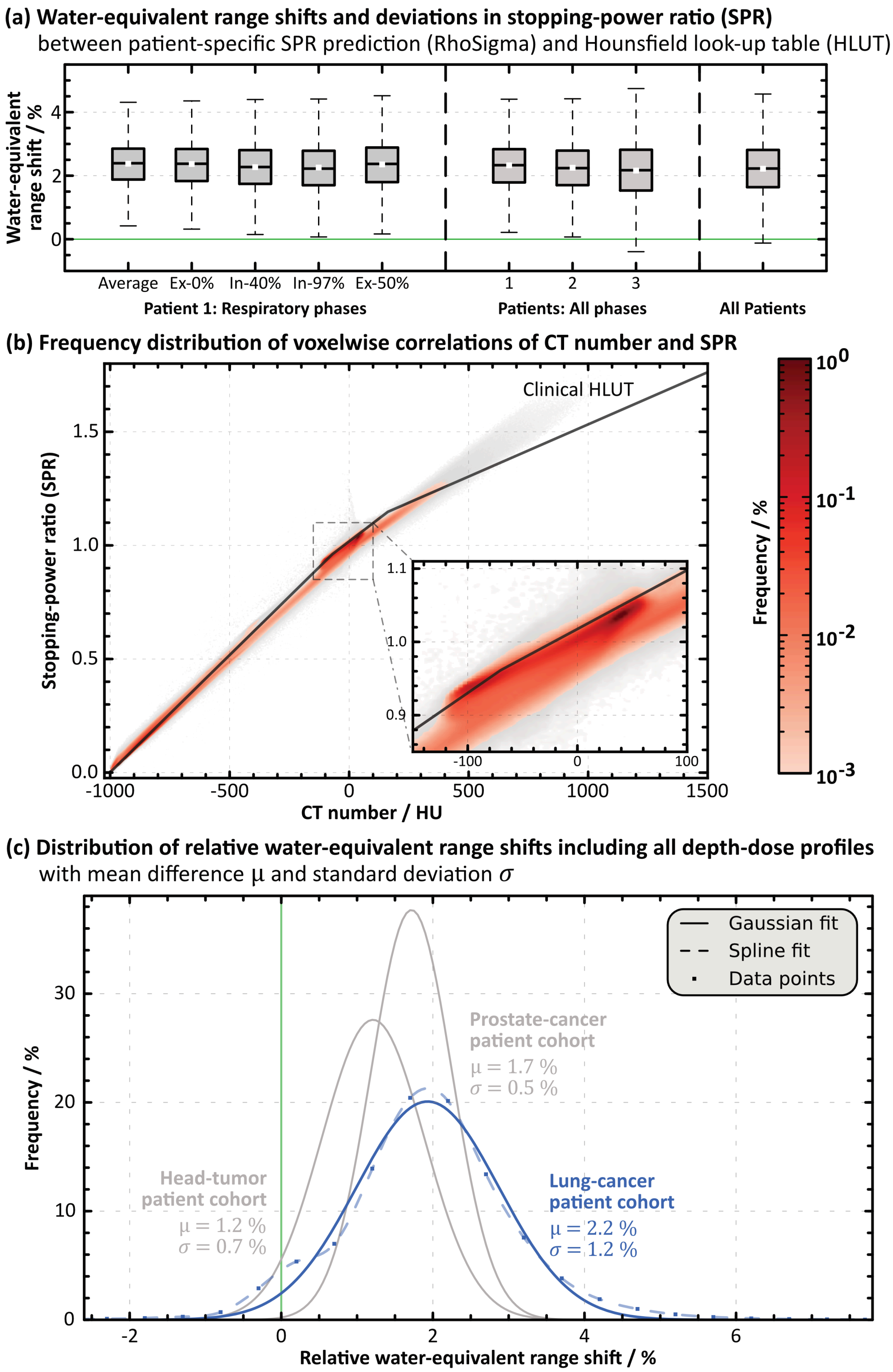

Figure 4: Water-equivalent range shifts and SPR distribution. Additionally, range shifts obtained in head-tumor and prostate-cancer patients were illustrated (3).

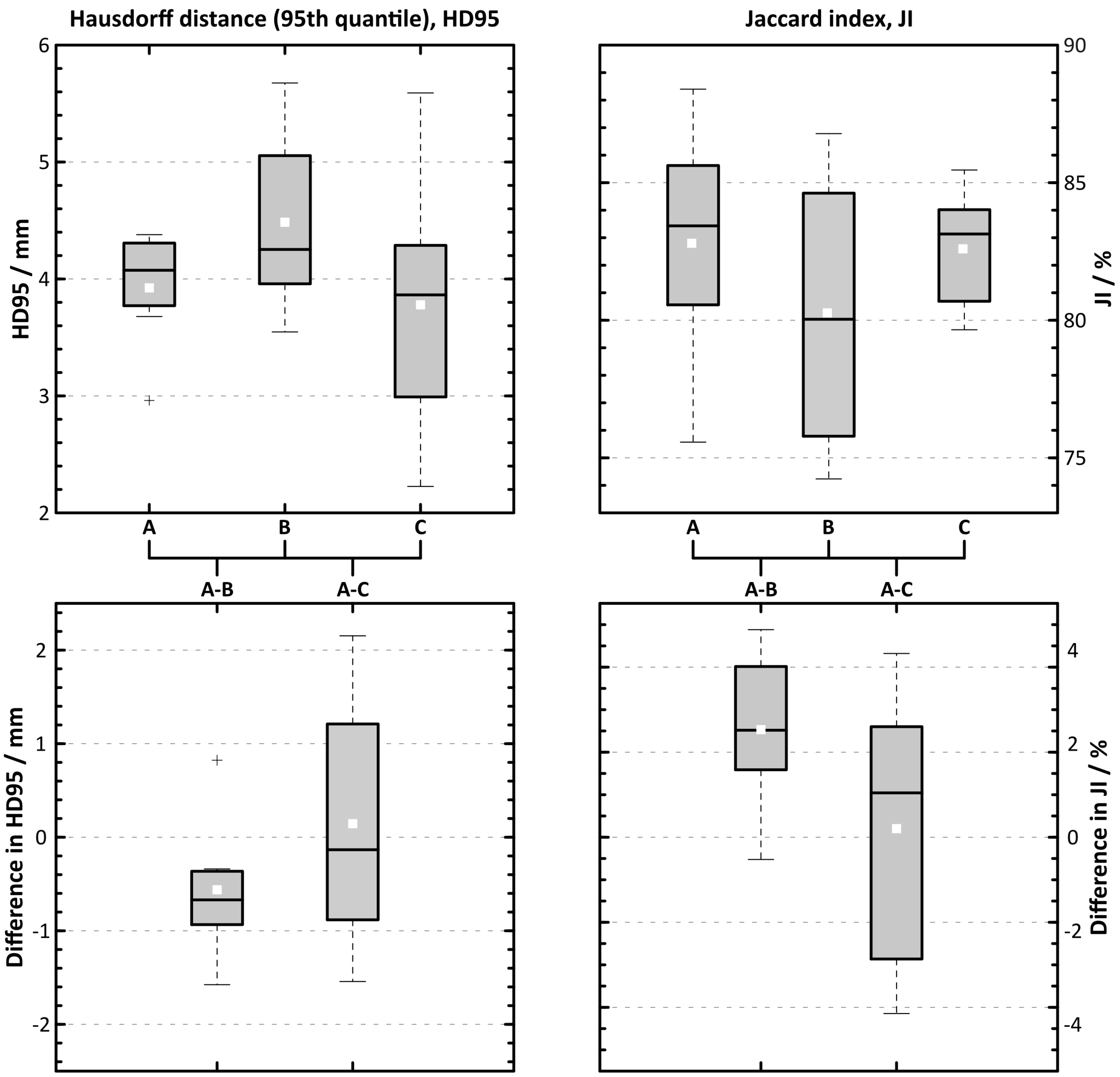

A ... Inter-modality variability between **79 keV pseudo-monoenergetic CT datasets (MonoCT)** and a combination of **relative-electron-density (RED) and 79 keV relative-cross-section (RCS) datasets.** Repeated contours of the gross tumor volume (GTV) were fused.

B ... Intra-observer variability on **79 keV MonoCT datasets**

C ... Intra-observer variability on a combination of **RED and 79 keV RCS datasets**

Figure 5: Intra-observer variability of GTV delineation.